PCCP

PAPER

View Article Online
View Journal | View Issue

Cite this: *Phys. Chem. Chem. Phys.*, 2015, **17**, 16991

NMR study of $Ba_8Cu_5Si_xGe_{41-x}$ clathrate semiconductors

Ali A. Sirusi,*[a] Joseph H. Ross Jr.,[ab] Xinlin Yan[c] and Silke Paschen[c]

Received 3rd May 2015,
Accepted 1st June 2015

DOI: 10.1039/c5cp02575c

www.rsc.org/pccp

We have performed ^{63}Cu, ^{65}Cu, and ^{137}Ba NMR on $Ba_8Cu_5Si_xGe_{41-x}$, a series of intermetallic clathrates known for their potential as thermoelectric materials, in order to investigate the electronic behavior of the samples. The spectra and spin–lattice relaxation times were measured at 77 K and 290 K for the entire composition range $0 \leq x \leq 41$. Magnetic and quadrupole shifts and relaxation rates of the Cu NMR data were extracted, and thereby carrier-induced metallic contributions identified. The observed shifts change in a nonlinear way with increasing Si substitution: from $x = 0$ to about 20 the shifts are essentially constant, while approaching $x = 41$ they increase rapidly. At the same time, Ba NMR data indicate greater Ba-site participation in the conduction band in $Ba_8Cu_5Si_{41}$ than in $Ba_8Cu_5Ge_{41}$. The results indicate surprisingly little change in electronic features *vs.* Si content for most of the composition range, while $Ba_8Cu_5Si_{41}$ exhibits enhanced hybridization and a more metallic framework than $Ba_8Cu_5Ge_{41}$.

1 Introduction

In recent years, highly efficient thermoelectric materials have been in demand to convert and harvest waste energy.[1,2] Among them intermetallic clathrates have gained great attention due to high thermoelectric efficiency[3–7] and other interesting physical properties such as glass-like thermal conductivity, superconductivity, and magnetism.[6,8–11] There have been many efforts to study $Ba_8Ga_{16}Ge_{30}$ and similar ternary semiconducting clathrates since they can have large thermoelectric figures of merit,[3–5] $ZT \approx 1$. The figure of merit is defined as $ZT = \frac{S^2\sigma T}{\kappa}$, where S is the Seebeck coefficient, σ is the electrical conductivity, κ is the thermal conductivity, and T is the temperature. Among these, it is the observed very low κ that is the principal source of the enhanced ZT.

Slack[12] first introduced the phonon-glass electron-crystal (PGEC) concept in which such compounds scatter phonons like an amorphous glass, and at the same time have charge carrier mobilities more like what is expected in a perfect crystal. Clathrates have large cages which can host electropositive guest atoms such as Ba, Eu, and Sr, and there is a general belief that the PGEC concept may apply to clathrates through anharmonic "rattling" guest atoms scattering phonons and thereby producing low thermal conductivity.[6,8,9] On the other hand, recent studies have connected the low thermal conductivity to intrinsic propagation behavior of low-velocity phonons in these structures.[13] $Ba_8Cu_5Ge_{41}$ is presumably in this category as its low thermal conductivity does not seem to be connected to large off-center Ba motion.[14] The Si analog, $Ba_8Cu_5Si_{41}$, has the potential to become a low-cost substitute for these materials.[15]

A recent comprehensive study[16] of the mixed alloys $Ba_8Cu_5Si_xGe_{41-x}$ showed that indeed small-x compositions have reduced κ and hence enhanced ZT due to alloy scattering, however compositions in a relatively narrow range near $x = 18$ exhibit an anomalous enhancement of κ as well as reduced carrier densities. On the other hand approaching full Si substitution, ZT is reduced due to electronic effects as the native carrier densities become large. Here we report the results of NMR studies to better understand these changes in electronic behavior. NMR shifts can be particularly sensitive to hybridization effects in the conduction and valence bands, and we find that with x increasing through the $x = 18$ composition there is very little change in such behavior, however approaching $Ba_8Cu_5Si_{41}$ the behavior changes rapidly as the framework becomes more metallic as observed both by Cu and Ba NMR.

2 Experiment

2.1 Synthesis and sample characterization

The $Ba_8Cu_5Si_xGe_{41-x}$ compounds studied here came from the same batch for which the preparation was described in ref. 16. The synthesis involved melting the pure-elements, followed by annealing and hot pressing. Powder X-ray diffraction (XRD) and analysis provided full structural details of the samples, and dispersive X-ray spectroscopy was measured to determine the

[a] *Department of Physics and Astronomy, Texas A&M University, College Station, Texas 77843, USA. E-mail: alisirusi@tamu.edu*
[b] *Department of Materials Science and Engineering, Texas A&M University, College Station, Texas 77843, USA*
[c] *Institute of Solid State Physics, Vienna University of Technology, Wiedner Hauptstraße 8-10, 1040 Vienna, Austria*

compositions of the samples (nominal x = 0, 3, 6, 10, 13, 18, 25, 35, 41) as reported in ref. 16. In this work we will denote the samples as Si(x). The type-I clathrate structure, common to all compositions examined here, has 46 Cu/Ge/Si framework atoms per unit cell. In addition 8 Ba guest atoms are situated on two cage sites: 2a (smaller dodecahedral cages) and 6d (tetrakaidecahedral cages).[5] It has been shown[16,17] at least for the end compositions (x = 0, 41), that Cu atoms occupy exclusively the 6c framework site (sometimes alternatively denoted as 6d, ref. 16).

The previous measurements[16] also included detailed transport results, among which the Hall-effect carrier densities will be used here. Note that the X-ray refinements show that the low Si content samples include small densities of vacancies in contrast to the Si-rich side where there are no vacancies. This is typical of Si and Ge clathrates: the spontaneously formed vacancies tend to enforce electron balance (Zintl concept[18]) and thereby lead to reduced carrier concentration. The previous results also showed that, while the lattice constants of the compounds decease linearly with increasing Si content, some internal parameters such as the Si occupation at the 24k site show nonlinear behavior.

2.2 NMR measurements

NMR experiments were carried out using a custom-built pulse spectrometer at a fixed field of 9 T. ^{63}Cu, ^{65}Cu, and ^{137}Ba spectra were measured with CuCl solid and aqueous $BaCl_2$, respectively, as the standard references relative to which all NMR shifts are reported. The powder samples were mixed with crushed quartz to allow for rf penetration. Measurements of Cu NMR utilized spin echo integration *vs.* frequency to record the quadrupole-broadened NMR spectra, whereas the Ba NMR spectra were obtained by using CPMG sequences[19] where the echo integrals were achieved at each frequency by summing all consecutive echoes in one CPMG sequence. Fitting of the NMR line-shapes was performed using the Dmfit package.[20]

NMR spin–lattice relaxation measurements were performed for low-temperature central transitions, with the relaxation time, T_1, as a fitted value based on a magnetic relaxation mechanism using a standard multi-exponential function for recovery of the central transition.[21,22] The quadrupole relaxation process entails a different relaxation function, and therefore an overall scaling of the quadrupole values of T_1. However this does not affect the dynamical fitting parameters described below. The fitted values will be identified for the 3 nuclei as $^{63}T_1$, $^{65}T_1$, and $^{137}T_1$. In the analysis, we used nuclear moment values reported in ref. 23 (^{63}Cu, $\gamma = 7.111789 \times 10^7$ rad s^{-1} T^{-1} and $Q = -22.0$ fm^2; ^{65}Cu, $\gamma = 7.60435 \times 10^7$ rad s^{-1} T^{-1} and $Q = -20.4$ fm^2).

3 Results and analysis

Fig. 1 shows ^{63}Cu spectra of the nine $Ba_8Cu_5Si_xGe_{41-x}$ samples obtained at room temperature. The scale is the total shift, defined as $\Delta f/f_0$ where f_0 is the standard reference frequency, and it includes both magnetic and electric quadrupole parts. Similar spectra (not shown) were obtained at 77 K, and for ^{65}Cu at both temperatures. The line-shapes are m = 1/2 to −1/2 transitions as reported in previous studies[24] for I = 3/2 Cu nuclei.

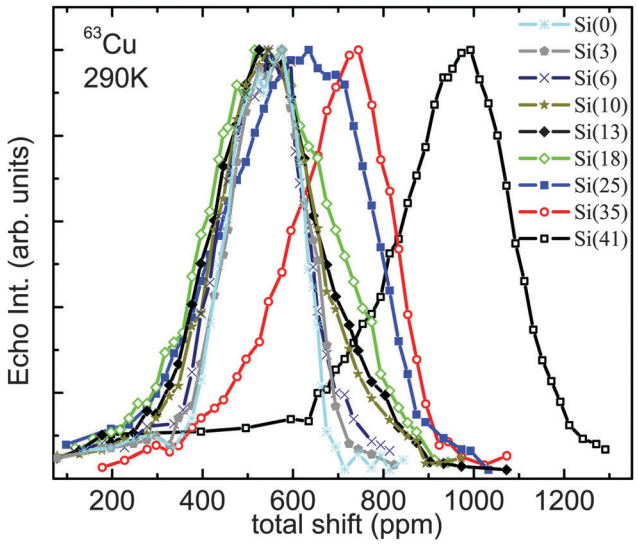

Fig. 1 ^{63}Cu spectra measured at room temperature for all investigated $Ba_8Cu_5Si_xGe_{41-x}$ samples.

By examination of ^{63}Cu and ^{65}Cu line-shapes we separated the magnetic and quadrupole shift contributions for each sample. Center of mass magnetic and quadrupole shifts were separated by using both the ^{63}Cu and ^{65}Cu centers of gravity and the relation $\Delta f/f_0 = \delta + BQ^2$, where δ is the magnetic shift (paramagnetic sign, by convention[23]), B is a constant, and Q is the quadrupole moment. Fig. 2 shows the resulting magnetic shifts. The quadrupole shifts due to the second-order quadrupole mechanism give small negative shifts less than −3 kHz (or −30 ppm), similar to the results of ref. 24 for $Ba_8Cu_yGe_{46-y}$ samples. The net magnetic shift δ can be further

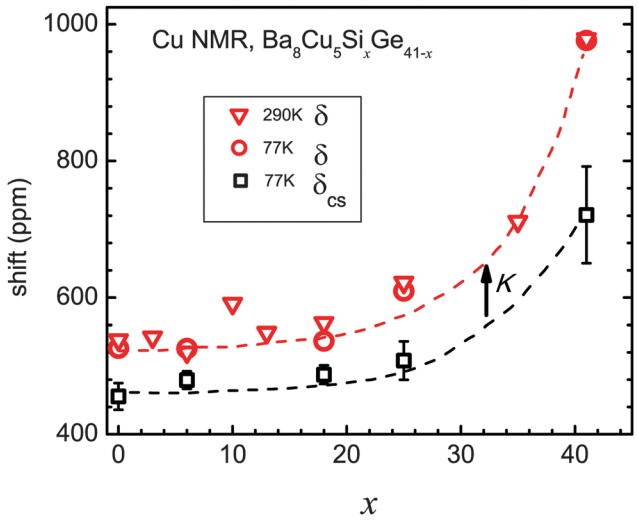

Fig. 2 Magnetic shifts (δ, open circles and triangles at 77 K and 290 K, respectively) and chemical shift component (δ_{cs}, open squares) as a function of Si content, plotted for Cu NMR in $Ba_8Cu_5Si_xGe_{41-x}$ at 77 K. Note that the Knight shift is defined as $K = \delta - \delta_{cs}$ (vertical arrow), as described in the text. The dashed lines are guides to the eyes.

separated[21,25] into a Knight shift and chemical shift ($\delta = K + \delta_{cs}$), where here we identify δ_{cs} as the contribution due to orbital effects, whereas K is due to conduction electron spins (and will depend on sample doping). The separation of these terms will be discussed further below. As seen in Fig. 2, δ is approximately independent of x up to Si(25), but it increases rapidly with x approaching the Si(41) composition, indicating electronic behavior that is very sensitive to x close to this composition extreme.

The extracted spin–lattice relaxation rates ($1/T_1$) can also be separated into two terms[22,24] by using the characteristic Q and γ dependencies. These terms are (1) a phonon contribution (quadrupole mechanism) which obeys $1/T_{1Q} \propto Q^2$ and (2) a carrier dominated term (magnetic term) which obeys $1/T_{1M} \propto \gamma^2$. $1/TT_{1M}$ for the samples obtained from this procedure at 77 K and room temperature are shown in Fig. 3(a). The inset in this figure shows $^{63}T_1/^{65}T_1$ plus the ratios of nuclear constants which indicate the dominant relaxation mechanism. If the quadrupole mechanism dominates, $^{63}T_1/^{65}T_1$ will be close to $(^{65}Q/^{63}Q)^2$, and the inset shows that this occurs for Si(0) up to Si(18) at 290 K. Fig. 3(b) shows the separated $1/T_{1Q}T$ for Si(0), Si(6), and Si(18) along with data for $Ba_8Cu_yGe_{46-y}$ (y = 4, 5.3, 6) as reported in ref. 24. The quadrupole rates are comparable in size and are typical for normal phonon behavior, which rise with temperature as shown schematically by the dashed line.

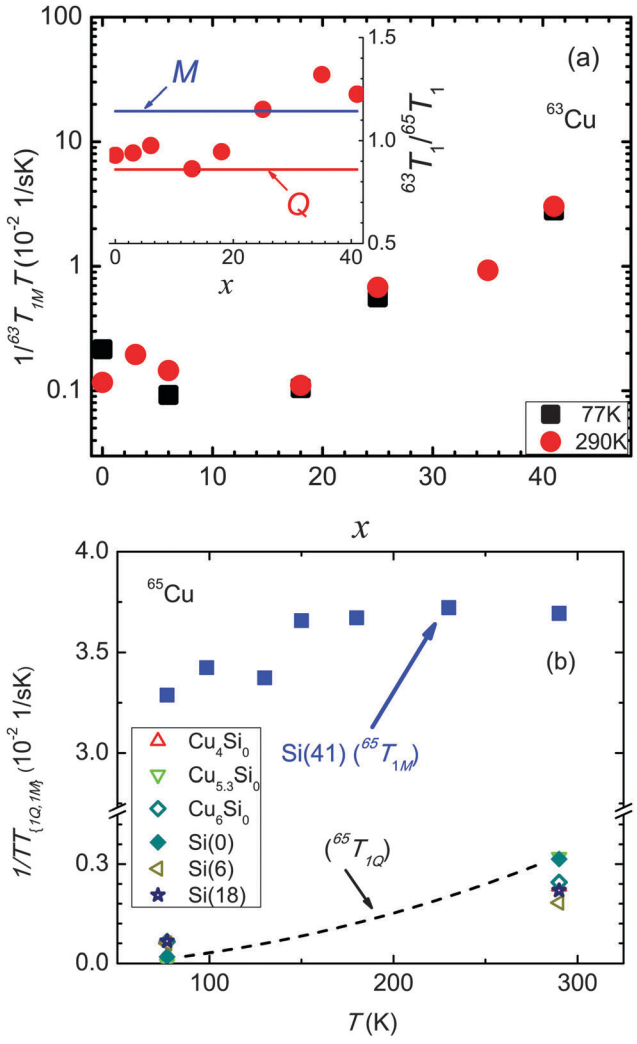

Fig. 3 (a) Magnetic spin–lattice relaxation contribution $1/TT_{1M}$ as function of Si content in $Ba_8Cu_5Si_xGe_{41-x}$ at 77 K and 290 K. The inset shows the $^{63}T_1/^{65}T_1$ ratio at 290 K with the magnetic ($^{63}T_1/^{65}T_1 = (^{65}\gamma/^{63}\gamma)^2$) values and quadrupolar ($^{63}T_1/^{65}T_1 = (^{65}Q/^{63}Q)^2$) values, labeled M and Q, respectively. (b) Quadrupole contribution $1/TT_{1Q}$ *vs.* temperature for Si(0), Si(6), Si(18) and the $Ba_8Cu_yGe_{46-y}$ (y = 4, 5.3, 6) samples from ref. 24. For comparison $1/TT_{1M}$ of the Si(41) sample is also plotted.

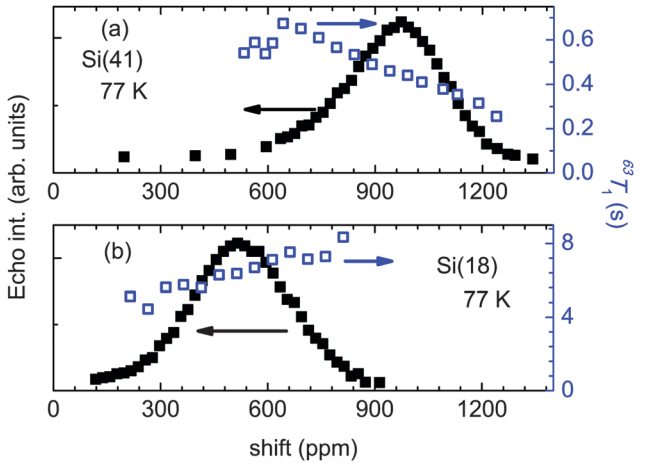

Fig. 4 ^{63}Cu NMR spectra and $^{63}T_1$ data *vs.* shift for (a) Si(41) and (b) Si(18) samples at 77 K.

It is noted that the relaxation rates used in the analysis were obtained at the maximum intensity points of the line-shapes although we do observe that T_1 changes across the lines. This is shown in Fig. 4 for Si(41) and Si(18), giving the measured T_1 as a function of frequency. These frequency dependencies can be understood as due to distributions of Si/Ge and Cu atoms in the vicinity of the Cu sites. These random distributions of framework atoms also cause line-shape broadening. To quantify this aspect the FWHMs of the ^{65}Cu line-shapes obtained by fitting to a Gaussian function at room temperature are shown in Fig. 5. The widths increase with increasing Si content up to Si(25) which is related to the random distribution of Si/Ge atoms on the 24k site which is the position of the nearest neighbors to Cu at the 6c site. The width is the largest for Si(25) since it has an equal Si/Ge 24k occupancy ratio consistent with a random distribution. There is also an overall increase in width going from Si(0) to Si(41), due to increased electric field gradients (EFG)'s related to the gradual decrease in the lattice parameter.

$1/T_{1M}$ at the line-center position was separated at 77 K and at room temperature for the 5 samples for which the carrier densities were also previously measured.[16] The results show that $T_{1M}T \approx$ constant, as expected for a relaxation mechanism dominated by conduction electrons. Previously[24] it was shown that for 3 samples of $Ba_8Cu_yGe_{46-y}$ (y = 4, 5.3, 6) with different carrier densities, the shift could be treated as $\delta = \delta_{cs} + K$, with δ_{cs} = 475 ppm, and with the product $K^2T_{1M}T \approx 1.2 \times 10^{-6}$ sK. The latter is the Korringa product[19] for metallic NMR shifts, with the measured value somewhat reduced relative to the value $K^2T_{1M}T = 3.73 \times 10^{-6}$ sK for metals in the absence of

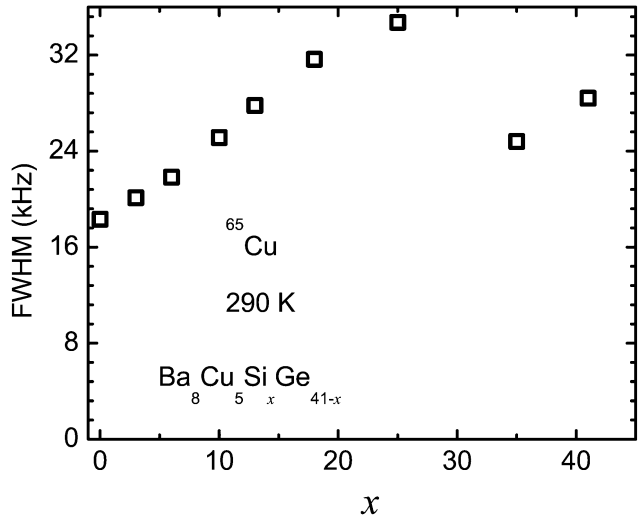

Fig. 5 FWHM of ^{65}Cu NMR line of $Ba_8Cu_5Si_xGe_{41-x}$ samples at room temperature.

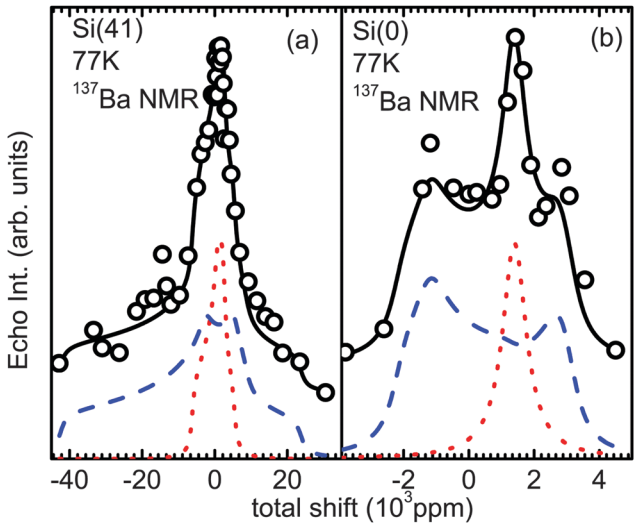

Fig. 6 ^{137}Ba NMR spectra measured at 77 K, along with fitted spectra (solid curves), showing two fitted sites: (1) the dotted curve (site A) and (2) the dashed curve (site B) as explained in the text. (a) Spectrum of Si(41) sample. (b) Spectrum of Si(0) sample.

electron–electron interactions. The small difference is similar to results in Si:P, where is was attributed to the presence of a small amount of disorder at the bottom of the conduction band.[24] For the present $Ba_8Cu_5Ge_{41}$ sample (Si(0)), assuming δ_{cs} = 475 ppm (77 K data) also yields $K^2T_{1M}T = 1.2 \times 10^{-6}$ sK, identical to the results obtained for previous samples. Using this value for the Korringa product, and thereby calculating K from the extracted T_{1M} values, we find that δ_{cs} increases with the Si content to 536 ppm for Si(25), and to 790 ppm for Si(41). Alternatively, assuming a non-reduced $K^2T_{1M}T = 3.73 \times 10^{-6}$ sK, somewhat smaller δ_{cs} values are obtained; the resulting two sets of values are plotted in Fig. 2 as the error-bar limits. Clearly, both δ_{cs} and K are nearly constant as the Si content increases to x = 25, indicating similar electronic behavior for these samples. On the other hand significantly larger shifts in Si(41) indicate a modification of the conduction/valence band configuration involving Cu orbitals at larger Si contents. This is true for both the metallic shift and δ_{cs} contributions for Si(41) (K is seen as the difference between δ and δ_{cs} plotted in Fig. 2).

^{137}Ba NMR spectra for the Si(0) and Si(41) samples at 77 K are shown in Fig. 6. These spectra were fitted as powder patterns assuming two sites: a narrow line (site A) and a broad line (site B). Similar to the Cu NMR results, these fits yield separate magnetic shifts (δ) and second-order quadrupole components. Due to the line widths we included only isotropic magnetic shifts in the fits. The Si(0) middle peak is narrow so we assumed site A to have zero EFG, and fit it to a Lorentzian function. The extracted spectral weight ratios A/B of the two fitted lines for Si(0) and Si(41) are 0.337 and 0.319. In type-I clathrates the expected ratio for the Ba sites 2a and 6d is 2/6 = 0.333, in agreement with the fitted ratios if site A is assigned to Ba atoms in the smaller cage. The fitting parameters are given in Table 1. Note that the smaller EFGs for site A in both cases match the more symmetric environment of the smaller cage as expected (ν_Q is related to the EFG through $\nu_Q = 3eQV_{zz}/[2I(2I-1)h]$ where V_{zz} is the largest principal EFG tensor component and I is the nuclear spin, while η_Q is defined as $\eta_Q = [V_{xx} - V_{yy}]/V_{zz}$). Moreover, the larger EFGs obtained for Si(41) correspond to its lower lattice constant compared to Si(0).

Table 1 ^{137}Ba NMR parameters obtained from fitting the Si(0) and Si(41) results at 77 K, along with the measured T_1. The definitions of the parameters are given in the text

	δ (ppm)	ν_Q (MHz)	η_Q	$^{137}T_1$ (ms)
Site A Si(0)	1393	0	0	1042
Site B Si(0)	1294	4 ± 0.05	0.18 ± 0.02	
Site A Si(41)	1890	4.8 ± 0.05	0.7 ± 0.02	180
Site B Si(41)	1825	11.77 ± 0.06	0.71 ± 0.02	

The Ba NMR T_1 values at the narrow peak positions are also given in Table 1. Similar to measured ^{135}Ba and ^{137}Ba relaxation rates in type-I $Na_xBa_ySi_{46}$ and chiral $Ba_{24}Ge_{100}$ clathrates, we assume that $^{137}T_1$ is dominated by the Korringa magnetic behavior.[26,27] The larger shift and shorter $^{137}T_1$ for Si(41) clearly indicates more metallic behavior for this composition. Assuming that the 500 ppm shift difference between Si(0) and Si(41) samples is entirely due to a Knight shift for the Si(41) sample, using $^{137}T_1$ of Table 1 the Korringa product $K^2T_1T = 3.5 \times 10^{-6}$ sK is obtained, slightly smaller than 21×10^{-6} sK expected for ^{137}Ba without electron–electron interactions. It is worth to mention that the magnetic shifts of the Si(0) and Si(41) samples are much smaller than in the superconductor[26] clathrate $Na_xBa_ySi_{46}$ (5930 ppm at 4.2 K)[26] and Ba metal[28,29] (4030 ppm at room temperature). However the enhanced Korringa contribution for Ba in $Ba_8Cu_5Si_{41}$ demonstrates a significantly greater participation of Ba in the conduction band in this material than in $Ba_8Cu_5Ge_{41}$.

As noted above, there is a small vacancy density in the Ge-rich compositions. XRD showed that this occurs appreciably only in the Si(0) and Si(3) samples,[16] which have 0.1 vacancies per cell on 6c framework sites. This will affect the NMR resonance

for ions in the close vicinity of vacancies. The immediate neighbors of these sites are 24k framework sites, which are not occupied by Cu, but those Ba and Cu ions occupying the same cage might also exhibit a weak split-off resonance. This was not seen in measurements for these two compositions, and it could be that these sites are out of the measurement range as sometimes occurs near defects; but however the main NMR shifts will not be affected.

4 Discussion

The Knight shift for metals can be calculated according to[21]

$$K_{\mathrm{th}} = \mu_{\mathrm{B}} g_{\mathrm{tot}}(E_{\mathrm{F}}) B_{\mathrm{HF}} \frac{g_{\mathrm{s}}}{g_{\mathrm{tot}}}, \qquad (1)$$

where B_{HF} is the hyperfine field, assumed dominated by the s-contact interaction, $g_{\mathrm{tot}}(E_{\mathrm{F}})$ is the density of states at the Fermi level and $g_{\mathrm{s}}/g_{\mathrm{tot}}$ is the ratio of partial density of states of the local s orbital to the total $g(E_{\mathrm{F}})$. In the effective-mass approximation, assuming a parabolic band edge, $g_{\mathrm{tot}}(E_{\mathrm{F}}) = (3n/\pi^4)^{1/3} m^*/\hbar^2$. Here we used the atomic-based[21] B_{HF} = 260 T for Cu.

Table 2 shows E_{F} and Cu Knight shift (K_{th}) values obtained from this calculation, the latter made with the assumption that $g_{\mathrm{s}}/g_{\mathrm{tot}} = 1$ in eqn (1), and with g_{tot} calculated per unit cell. Using K from the analysis above ($\delta - \delta_{\mathrm{cs}}$, values plotted in Fig. 2), we obtain the ratio K/K_{th} given in Table 2. K/K_{th} therefore corresponds to $g_{\mathrm{s}}/g_{\mathrm{tot}}$, the number of s states for a given Cu atom relative to the number of conduction states in the cell as a whole. For example, assuming that conducting states have the ideal sp^3 hybridization and are equally distributed among the 46 framework atoms, this ratio will be (1/4/46) = 0.0054. The smaller values displayed in Table 2 indicate a reduced Cu s-contribution to the conduction band edge.

Previously[24] $g_{\mathrm{s}}/g_{\mathrm{tot}}$ was calculated to be 0.0014 based on first-principles methods for $Ba_8Cu_{5.3}Ge_{40.7}$; the value 0.0013 found here for $Ba_8Cu_5Ge_{41}$ (Si(0) sample) is in excellent agreement. The calculation for $Ba_8Cu_{5.3}Ge_{40.7}$ also indicated[24] that up to about 0.2 eV above the conduction band edge the effective mass approximation works well, with little change in the partial densities of states, while at higher energies multiple bands begin to participate. As shown in Table 2, this condition applies to the Si(0) and Si(18) compositions since they have sufficiently low carrier densities; similar values of K/K_{th} for these compositions, as well as of m^*/m_{e}, provide an indication that the conduction states remain essentially unchanged with Si substitution up to at least x = 18. This behavior matches the nearly-constant Cu chemical shifts (Fig. 2) across this range.

For Si(41) the measured carrier densities place E_{F} further into the conduction band than for the other samples, and the measured Cu K is correspondingly considerably larger. Note that DFT calculations[16] for $Ba_8Cu_6Ge_{40}$ do not show a semiconducting gap as is found for $Ba_8Cu_{6-x}Ge_{40+x}$ (ref. 24 and 30). The accurate estimation of band gaps in such calculations can be difficult but we tentatively conclude that the more metallic properties of Si(41) are indeed an indication of semimetallic behavior, and that the upturn in NMR shift close to full Si substitution corresponds to a crossing of states near E_{F} for compositions in this range. The chemical shifts reinforce this conclusion as discussed below.

The Cu chemical shift $\delta_{\mathrm{cs}} \approx 700$ ppm for Si(41) is at the upper range of shifts observed in Cu molecular systems.[31] There are not many semiconductors for which a Cu δ_{cs} has been identified unambiguously. The cubic phase Cu_2Se has a vanishing K contribution by symmetry, and exhibits[32,33] δ_{cs} = 220 ppm. The enhanced δ_{cs} in $Ba_8Cu_5Si_{41}$ is due to the paramagnetic mechanism as described below.

The chemical shift can be expressed to include a diamagnetic (shielding) and paramagnetic term,[25] of which the latter is expressed as

$$\delta_{\mathrm{para}} = \frac{{\mu_{\mathrm{B}}}^2}{2} \sum_{i,j} \frac{\left\{ \left\langle \psi_j \middle| L_z \middle| \psi_i \right\rangle \left\langle \psi_i \middle| L_z / r^3 \middle| \psi_j \right\rangle + \mathrm{c.c.} \right\}}{E_i - E_j}, \qquad (2)$$

where ψ_i is a state in the conduction band, ψ_j is a filled state, and E_i and E_j are the corresponding energies. The angular momentum matrix elements in the numerator are nonzero when states including the same local orbital are connected. This corresponds to hybridization of states across the gap. Hence, the enhanced δ_{cs} in Si(41) shows that Cu p states become more distributed between conduction and valence bands. This gives a more specific picture of the electronic changes responsible for the non-monotonic electronic transport previously observed.

Table 2 Measured charge carrier densities (n) and effective masses (m^*) from ref. 16 with calculated Fermi energies (E_{F}), theoretical Cu Knight shifts (K_{th}), and K/K_{th} ratios from experiment. The latter is equivalent to $g_{\mathrm{s}}/g_{\mathrm{tot}}$, as explained in the text

Compounds	n (10^{21} cm^{-3})	m^*/m_{e}	E_{F} (eV)	K_{th} (%)	K/K_{th} ($g_{\mathrm{s}}/g_{\mathrm{tot}}$)
Si(0)	0.278	1.13	0.137	5.6	0.0013
Si(6)	0.855	1.44	0.228	10.2	0.0004
Si(18)	0.179	1.16	0.100	4.7	0.0010
Si(25)	0.809	1.35	0.235	8.9	0.0011
Si(41)	2.142	1.65	0.367	14.5	0.0017

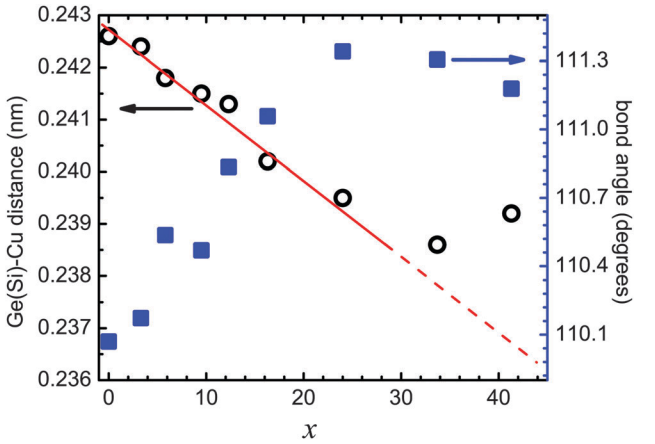

Fig. 7 Cu-nearest neighbor distance (open circles) and bond angle (solid squares). Angles are the larger of two values as explained in the text. Values from ref. 16. The dashed and solid lines are guides to the eyes.

We plot the Cu-ion nearest neighbor distances and bond angles from the XRD parameters[16] in Fig. 7, illustrating changes in the Cu local environment, with Cu atoms on the 6c sites, each enclosed by 4 nearest neighbors on 24k sites. The symmetry is nearly that of a regular tetrahedron (ideal bond angle 109.5°) distorted to give one smaller and one larger angle; the larger angle is plotted in the figure. The strong non-linearity in both plots is related to previously identified structure features[16] connected to a change in the transport properties in going from Si(0) to Si(41). The monotonic decrease in bond length for most of the range corresponds to the decrease in the measured lattice constant. However this trend is reversed, with a longer bond for Si(41), apparently a weakening of the bond which coincides with the framework becoming more metallic, and the large increase in Cu NMR shifts. This also coincides with a stronger Ba participation in the conduction band, as seen from enhanced Ba NMR shifts and $1/T_1$.

5 Conclusions

In summary, we have measured ^{63}Cu, ^{65}Cu, and ^{137}Ba NMR on Si-substituted $Ba_8Cu_5Ge_{41}$ clathrates, across the composition range to $Ba_8Cu_5Si_{41}$. We determined separately the chemical shifts and carrier-related Knight shifts. Surprisingly, the Cu NMR indicates that the band-edge behavior and distribution of states within the valence and conduction band remains essentially constant up to nearly complete Si substitution, at least from the perspective of Cu local orbitals. However for compositions close to $Ba_8Cu_5Si_{41}$ a rapid increase in shifts is observed, as well as an increase in Ba metallic shifts, which we connected to a greater hybridization and more metallic behavior of the framework at this composition.

Acknowledgements

This work was supported by the Robert A. Welch Foundation (Grant No. A-1526) and the Austrian Science Fund (FWF project TRP 176-N22).

References

1 G. J. Snyder and E. S. Toberer, *Nat. Mater.*, 2008, **7**, 105.
2 L. E. Bell, *Science*, 2008, **321**, 1457.
3 J. Martin, H. Wang and G. S. Nolas, *Appl. Phys. Lett.*, 2008, **92**, 222110.
4 A. Saramat, G. Svensson, A. E. C. Palmqvist, C. Stiewe, E. Mueller, D. Platzek, S. G. K. Williams, D. M. Rowe, J. D. Bryan and G. D. Stucky, *J. Appl. Phys.*, 2006, **99**, 023708.
5 T. Takabatake, K. Suekuni, T. Nakayama and E. Kaneshita, *Rev. Mod. Phys.*, 2014, **86**, 669.
6 M. Christensen, S. Johnsen and B. B. Iversen, *Dalton Trans.*, 2010, **39**, 978.
7 H. Kleinke, *Chem. Mater.*, 2010, **22**, 604.
8 G. S. Nolas, J. L. Cohn, G. A. Slack and S. B. Schujman, *Appl. Phys. Lett.*, 1998, **73**, 178.
9 G. S. Nolas, J. L. Cohn, J. S. Dyck, C. Uher and J. Yang, *Phys. Rev. B: Condens. Matter Mater. Phys.*, 2002, **65**, 165201.
10 J. H. Ross, Jr. and Y. Li, *Nanoscale Magnetic Materials and Applications*, Springer, New York, 2009, ch. 4, p. 105.
11 F. M. Grosche, H. Q. Yuan, W. Carrillo-Cabrera, S. Paschen, C. Langhammer, F. Kromer, G. Sparn, M. Baenitz, Y. Grin and F. Steglich, *Phys. Rev. Lett.*, 2001, **87**, 247003.
12 G. A. Slack, *CRC Handbook of Thermoelectrics*, CRC Press, 1995.
13 S. Pailhès, H. Euchner, M. Giordano, V. R. Debord, A. Assy, S. Gomes, A. Bosak, D. Machon, S. Paschen and M. de Boissieu, *Phys. Rev. Lett.*, 2014, **113**, 025506.
14 S. Johnsen, M. Christensen, B. Thomsen, G. K. H. Madsen and B. B. Iversen, *Phys. Rev. B: Condens. Matter Mater. Phys.*, 2010, **82**, 184303.
15 X. Yan, M. Falmbigl, S. Laumann, A. Grytsiv, E. Bauer, P. Rogl and S. Paschen, *J. Electron. Mater.*, 2012, **41**, 1159.
16 X. Yan, E. Bauer, P. Rogl and S. Paschen, *Phys. Rev. B: Condens. Matter Mater. Phys.*, 2013, **87**, 115206.
17 S. Johnsen, A. Bentien, G. K. H. Madsen, M. Nygren and B. B. Iversen, *Phys. Rev. B: Condens. Matter Mater. Phys.*, 2007, **76**, 245126.
18 E. Zintl, *Angew. Chem.*, 1939, **52**, 1–6.
19 C. P. Slichter, *Principles of Magnetic Resonance*, Springer Verlag GmbH, 1996.
20 D. Massiot, F. Fayon, M. Capron, I. King, S. Le Calvé, B. Alonso, J.-O. Durand, B. Bujoli, Z. Gan and G. Hoatson, *Magn. Reson. Chem.*, 2002, **40**, 70.
21 G. Carter, L. Bennett and D. Kahan, *Prog. Mater. Sci.*, 1977, **20**, 1.
22 X. Zheng, S. Y. Rodriguez and J. H. Ross, Jr., *Phys. Rev. B: Condens. Matter Mater. Phys.*, 2011, **84**, 024303.
23 R. K. Harris and E. D. Becker, *J. Magn. Reson.*, 2002, **156**, 323.
24 J.-H. Chen, A. Sirusi Arvij, X. Zheng, S. Y. Rodriguez and J. H. Ross, Jr., *J. Alloys Compd.*, 2014, **593**, 261.
25 *Calculation of NMR and EPR Parameters: Theory and Applications*, ed. M. Kaupp, M. Bühl and V. G. Malkin, Wiley-VCH, 1st edn, 2004.
26 F. Shimizu, Y. Maniwa, K. Kume, H. Kawaji, S. Yamanaka and M. Ishikawa, *Phys. Rev. B: Condens. Matter Mater. Phys.*, 1996, **54**, 13242.
27 F. Kanetake, A. Harada, H. Mukuda, Y. Kitaoka, T. Rachi, K. Tanigaki, K. M. Itoh and E. E. Haller, *J. Phys. Soc. Jpn.*, 2009, **78**, 104710.
28 T. J. Rowland, *Phys. Rev.*, 1956, **103**, 1670.
29 G. A. Styles and G. Tranfield, *Phys. Lett. A*, 1974, **48**, 471.
30 S. Johnsen, A. Bentien, G. K. H. Madsen, B. B. Iversen and M. Nygren, *Chem. Mater.*, 2006, **18**, 4633.
31 R. J. Goodfellow, *Multinuclear NMR*, Springer US, 1987.
32 K. Becker and H. Schäfgen, *Solid State Commun.*, 1979, **32**, 1107.
33 A. A. Sirusi, J. H. Ross, Jr., S. Ballikaya and C. Uher, submitted.

